



30 deviations of the fitting residuals. The derived error in the Huggins band ($\sim 0.1\%$) is twice the OMPS
31 L1B measurement error. OMPS floor noise errors better constrains our retrievals, leading to improving
32 information content of ozone and reducing fitting residuals. The final precision of the fitting residuals
33 is less than 0.1% in the low/mid latitude, with ~ 1 degrees of freedom for signal for the tropospheric
34 ozone, meeting the general requirements for successful tropospheric ozone retrievals.

35 1. Introduction

36 Atmospheric ozone has very different roles depending upon its altitude. About 90% of the total
37 ozone is in the stratosphere, protecting the Earth's life from harmful solar ultraviolet (UV) radiation
38 that can cause skin cancer and immune system suppression. The remaining 10% in the troposphere
39 shows dangerous effects as a major component of photochemical smog at surface level and as a short-
40 lived greenhouse gas in the upper troposphere, whereas in the middle troposphere it plays a beneficial
41 role in chemically cleaning the atmosphere as a precursor of hydroxyl radicals (OH). Therefore, vertical
42 ozone profiles should be monitored to improve our understandings of the chemical and physical
43 functions of this important trace gas. Space-based monitoring of ozone profiles including the
44 troposphere from backscattered UV radiation has been available since the launch of Global Ozone
45 Monitoring Experiment (GOME) (European Space Agency, 1995) on board the Second European
46 Remote Sensing Satellite (ERS-2) in April 1995. Its successors continued the role of GOME for
47 atmospheric ozone monitoring with Scanning Imaging Absorption SpectroMeter for Atmospheric
48 ChartographY (SCIAMACHY) (Bovensmann et al., 1999) aboard the Environmental Satellite
49 (ENVISAT), GOME-2s (EUMETSAT, 2006) aboard the MetOp-A and MetOp-B, and Ozone
50 Monitoring Instrument (OMI) (Levelt et al, 2006) flown on the EOS Aura spacecraft. The good
51 performance of OMI ozone profile retrievals in both stratosphere and troposphere has been
52 demonstrated through extensive validation efforts using ozonesondes, aircraft, satellite data, and
53 ground-based total ozone data (Pittman et al., 2009; Liu et al., 2010b; Bak et al., 2013b; 2015; Huang
54 et al., 2017a,b). However, a portion of OMI radiance measurements has been affected by the partial
55 blockage of the instrument's entrance slit, a problem termed the row anomaly, which started in 2007
56 and grew serious in January 2009 (Schenkeveld, 2017). The Ozone Mapping and Profiler Suite (OMPS)
57 aboard the Suomi National Polar-Orbiting Partnership (NPP) satellite launched in 2011 (Flynn, et al.,
58 2014) represents the next generation of US instruments to continue the role of OMI in monitoring total
59 ozone and ozone vertical profiles, together with the TROPOspheric Monitoring Instrument
60 (TROPOMI) to be launched on board the Sentinel-5 Precursor satellite in 2017 (Veefkind et al., 2012).



61 OMPS is a sensor suite which consists of three instruments, the Nadir Mapper (OMPS-NM), the Nadir
62 Profiler (OMPS-NP), and the Limb Profiler (OMPS-LP). The OMPS-NM is designed to measure the
63 daily global distribution of total column ozone with an 110° cross-track field of view (FOV), similar to
64 OMI and the Total Ozone Monitoring Spectrometer (TOMS) series (Bhartia and Wellemeyer, 2002).
65 OMPS-NP is an ozone profiler sensor, measuring the vertical ozone profiles in the upper stratosphere,
66 similar to the Solar Backscatter Ultraviolet (SBUV/2) series (Bhartia et al., 2013). The OMPS-LP is
67 designed to measure ozone profiles in the stratosphere and upper troposphere at high vertical resolution,
68 similar to the Microwave Limb Sounder (MLS). Both OMPS-NP and OMPS-LP are ozone profile
69 sensors, but lack sensitivity to the troposphere due to the spectral coverage of 250-290 nm and the
70 viewing geometry, respectively. Therefore, OMPS-NM is the only candidate for global monitoring of
71 ozone profiles down to the troposphere even though its spectral resolution of 1.0 nm does not fully
72 resolve the ozone absorption band features in the Huggins band and its spectral coverage of 300-380
73 nm is insufficient to retrieve stratospheric ozone profiles. The retrieving of ozone profiles including
74 tropospheric ozone from OMPS-NM measurements has not yet been presented in the literature. The
75 present effort fills the gap between OMI and upcoming satellite observations.

76 The final goal of this study is to demonstrate the successful performance of ozone profiles and
77 tropospheric ozone retrievals from only OMPS-NM measurements. Thus, we refer to OMPS-NM
78 simply as OMPS hereafter. The retrieval algorithm used in this study is based on the Smithsonian
79 Astrophysical Observatory (SAO) ozone profile algorithm that was developed for GOME (Liu et al.,
80 2005) and OMI (Liu et al., 2010a). The SAO OMI algorithm is based on an optimal estimation inversion
81 (Rodgers, 2000) combined with accurate wavelength/radiometric calibration, forward model
82 simulation, and good a priori knowledge. This algorithm has been implemented for ozone profile and
83 SO₂ retrievals from GOME-2 instrument (Cai et al., 2011; Nowlan et al., 2011) and will be adapted to
84 ozone profile retrievals from upcoming geostationary UV/VIS spectrometers including the
85 Geostationary Environmental Monitoring Spectrometer (GEMS) (Bak et al 2013a) and Tropospheric
86 Emissions: Monitoring of POLLution (TEMPO) instrument (Chance et al., 2013, Zoogman et al., 2017)
87 for monitoring air quality over North America and East Asia, respectively. OMPS has a similar
88 instrument concept to OMI, GEMS, and TEMPO and hence the application of the similar retrieval
89 algorithms to these measurements will provide an excellent opportunity for long-term trend analysis of
90 ozone profiles, especially in the troposphere. The OMI algorithm is very similar to our OMPS algorithm,
91 but it needs additional optimization for OMPS. In this paper we focus largely on characterizing OMPS
92 measurements (1) through the cross-correlation between OMPS irradiances and a high-resolution solar
93 reference to be used in the verification of OMPS slit function measurements and the characterization of



94 the wavelength registration and (2) through extracting the systematic and random components of fitting
95 residuals between measured and calculated normalized radiances to be used in radiometric and
96 measurement error calibrations, respectively. Several companion papers to follow will deal with the
97 detailed error analysis, retrieval characteristics of the retrieved ozone profiles, and validation of
98 retrievals.

99 The paper is divided into four sections: First, we give a description of OMPS-NM Level 1B (L1B)
100 v2.0 data (Jaross, 2017) and the ozone profile algorithm in Sect. 2. Section 3 discusses the
101 wavelength/slit function calibrations and measurement corrections for radiance and measurement error,
102 respectively. Conclusions are in Sect. 4.

103

104 **2. Data and Method**

105 **2.1 OMPS measurements**

106 The Suomi NPP satellite is a NOAA/NASA scientific partnership, launched in 2011 into a 824 km sun-
107 synchronous polar orbit with ascending node equator-crossing time at 13:30 local time. Routine
108 operations began in 2012. Suomi NPP carries five instruments: The Visible/Infrared Imager Radiometer
109 Suite (VIIRS), the Cross-track Infrared Sounder (CrIS), the Advanced Technology Microwave Sounder
110 (ATMS), the Ozone Mapping and Profile Suite (OMPS), and the Clouds and the Earth Radiant Energy
111 System (CERES). OMPS is a key instrument on Suomi NPP. The sensor suite has both nadir and limb
112 modules. The nadir module combines two sensors: The Nadir Mapper for measuring total column ozone,
113 and the Nadir Profiler for ozone vertical profile. The Limb Profiler module is designed to measure
114 vertical ozone profiles with high vertical resolution from the upper troposphere/lower stratosphere to
115 the mesosphere. The OMPS-NM employs a 2-D CCD that samples spectrally in one dimension and
116 spatially in the other, similar to OMI. It has a 110° cross-track field of view, resulting in 2800 km
117 instantaneous swath coverage at the earth's surface; this is sufficient to provide daily global coverage.
118 It makes 400 swath lines per orbit with 36 cross-track measurements per swath line, resulting in a nadir
119 footprint of 50 km × 50 km in its nominal configuration. Note that OMPS L1B data used in this
120 investigation contain 36 cross-track pixels, because the L1B processing in the NASA Ozone SIPS
121 retains the two central (near-nadir) instantaneous fields of views (IFOVs, 30 km × 50 km and 20 km ×
122 50 km), without aggregating them into the nominal 50 km × 50 km pixel. The spectral coverage is from
123 300 to 380 nm with a spectral resolution of ~ 1.0 nm and a sampling of 0.42 nm. The OMPS level 0 to
124 1b processor was recently updated from version 1.0 to 2.0. The satellite measurements from the OMPS-



125 NM instrument used in this study are from version 2 of the NMEV-L1B data product (Jaross, 2017)
126 available from the NASA Goddard Earth Sciences Data and Information Services Center (GES
127 DISC). The data consist of calibrated Earth-view radiance and solar irradiance data measured by the
128 instrument between 300-380 nm. Seftor et al. (2014) documented many aspects of the previous version
129 of the dataset that remain the same, but a number of changes for the V2 dataset do reflect advances in
130 the characterization of the NM sensor (Seftor and Jaross, 2017) which are relevant to this study. These
131 are summarized as follows: 1) recalculation of instrument band-pass functions in the 300-310 nm region
132 affected by the dichroic element of the nadir instrument, 2) improved wavelength registration, 3) an
133 update to the instrument radiance calibration, and 4) improvement to the stray light correction. The
134 wavelengths below 302 nm are not used in this study, according to the recommendation of the OMPS
135 science team.

136 **2.2 OMPS simulations**

137 We use the Vector Linearized Discrete Ordinate Radiative Transfer (VLIDORT) model (Spurr, 2006;
138 2008) to simulate OMPS radiances. VLIDORT is also able to simulate the analytic derivatives of
139 radiance with respect to any atmospheric or surface parameter due to its full linearization capability.
140 The polarization of light is taken into account in VLIDORT calculation, but the Ring spectrum is
141 modeled using a single scattering RRS model (Sioris and Evans, 2000). We consider only Rayleigh
142 scattering (no aerosol) and ozone absorption (no other trace gases), with Lambertian reflectance
143 assumed for the surface and for clouds. Clouds are treated as a Lambertian reflector at cloud top, with
144 a fixed albedo of 0.8 unless it is fully cloudy so that the cloud albedo (>0.80) can be derived. Cloud
145 fraction is required to simulate partial clouds as the weighted average between clear and cloudy scenes
146 using the Independent Pixel Approximation (IPA). The forward model inputs used in VLIDORT are
147 listed in Table 1.

148 **2.3 OMPS ozone profile retrievals**

149 The inversion from Backscattered UV measurements to the state of the atmosphere is performed
150 using the well-known optimal estimation method (Rodgers, 2000). It calculates the a posteriori solution
151 by iteratively and simultaneously minimizing the cost function consisting of the sum of the squared
152 differences between measured and simulated radiances and between retrieved and a priori state vectors,



153 constrained by measurement error covariance matrix and a priori error covariance matrix. The a
 154 posteriori solution and cost function can be written:

$$155 \quad X_{i+1} = X_i + (K_i^T S_y^{-1} K_i + S_a^{-1})^{-1} [K_i^T S_y^{-1} (Y - R(X_i)) - S_a^{-1} (X_i - X_a)] \quad (1)$$

$$156 \quad \chi^2 = \left\| S_y^{-\frac{1}{2}} \{K_i(X_{i+1} - X_i) - [Y - R(X_i)]\} \right\|_2^2 + \left\| S_a^{-\frac{1}{2}} (X_{i+1} - X_a) \right\|_2^2. \quad (2)$$

157 The inputs to the optimal estimation are defined as follows. \mathbf{X} is the state vector to be retrieved,
 158 consisting of ozone profiles as well as other geophysical parameters and spectroscopic parameters
 159 affecting the observed radiances and hence the retrieval of ozone profile. The 24 partial columns of
 160 ozone in DU are retrieved at 25 pressure levels that are initially set to be $P_i = 2^{-i/2}$ atm for $i =$
 161 $0, 1, \dots, 23$ (1 atm = 1013.25 hPa) with the top of the atmosphere at 0.087 hPa for P_{24} . The geophysical
 162 parameters include effective surface albedo and cloud fraction. The calibration parameters consists of
 163 two wavelength shift parameters between radiances and irradiances and between radiances and ozone
 164 cross sections and two scaling parameters for the Ring effect that account for filling-in of Fraunhofer
 165 lines in the solar spectrum due to rotational Raman scattering and mean fitting residuals that may not
 166 be accounted for properly in radiometric calibration. The a priori data for ozone is one of the key optimal
 167 estimation inputs because the retrieval solution comes mainly from a priori information rather than
 168 measurement information where the instrument sensitivity to the true ozone profile is insufficient. The
 169 a priori value (X_a) and a priori error covariance (S_a) of ozone is taken from the tropopause-based ozone
 170 profile climatology that is optimized to represent the dynamical ozone variability in the upper
 171 troposphere and lower stratosphere (Bak et al., 2013b). The measurement vector Y is defined as the
 172 logarithm of the earthshine radiances normalized to the daily solar irradiance. S_y is a measurement
 173 error covariance matrix that is assumed to be a diagonal matrix with diagonal elements being the squares
 174 of the assumed measurement errors. We use OMI floor noise errors (0.4 % below 310 nm, 0.2 % above,
 175 Huang et al., 2017a) as our preliminary measurement constraint and then derive OMPS floor noise
 176 errors specified in Section 3.4. $R(X)$ is the calculated radiances corresponding to X . K is a weighting
 177 function matrix representing partial derivatives of the forward model with respect to the atmospheric
 178 parameters, $K_{ij} = \partial R_i(X) / \partial X_j$. More detailed descriptions can be detailed in Liu et al. (2010a).

179



180 **3. Results**

181 **3.1 Slit Function and Wavelength Calibration`**

182 It is essential to investigate the best knowledge of the instrument slit function to convolve a high-
183 resolution solar reference spectrum for wavelength calibration as well as to convolve high-resolution
184 trace gas cross sections for simulation of earthshine spectra. A triangular bandpass with a fixed
185 bandwidth of 1.1 nm has been typically used for Total Ozone Monitoring Instrument (TOMS), SBUV,
186 and SBUV/2 monochromators. Slit functions of spectrometers such as OMI and GOME1/2 have been
187 measured prior to launch using a tunable laser or analytically derived assuming a Gaussian-type shape
188 if measured slit functions are unavailable or inaccurate. The OMPS preflight slit functions were
189 measured for each CCD pixels (196 band centers and 36 cross-track positions), which has been adopted
190 and modified for OMPS trace-gas retrievals such as in Yang et al. (2013; 2014) and Gonzalez Abad et
191 al. (2016). The slit function modification is accomplished in the previous works (Yang et al., 2013,
192 2014) by stretching and shrinking the slit widths, i.e., by applying a wavelength-dependent scaling
193 factor to the OMPS measured slit functions. According to Yang et al. (2013; 2014), we fit the scaling
194 factor as a slit parameter so that variations in measured slit functions before and after launch could be
195 taken into account.

196 Figure 1a shows an example of measured OMPS slit functions at 320 nm, illustrating that their
197 shapes seem to be Gaussian and vary considerably over cross-track pixels, especially near the wings.
198 Note that the 36 cross-track positions are denoted from 1 at the left edge and 36 at the right edge. The
199 slit function shapes at 17th cross-track position are nearly consistent over wavelengths that we are
200 focusing on for ozone retrievals (Fig. 1.b). Figure 1c displays the full width at half maximum (FWHM)
201 including dependencies in both dimensions of the detector arrays. The spectral variation of the slit
202 widths is insignificant (FWHMs vary by less than 0.01 nm), whereas average slit widths vary
203 significantly across track by over 0.1 nm. This characteristic of measurement slit functions confirms
204 that we should consider their cross-track dependence for OMPS slit functions, but their wavelength
205 dependence is ignorable so that we can avoid the time-consuming convolution process.

206 We evaluate the usefulness of these measured slit functions for fitting both OMPS radiance and
207 irradiance against the analytical slit functions assusing both standard Gaussian and supper Gaussian
208 distributions. We note all the Gaussian shapes used in this analysis are assumed to be symmetric. The
209 Gaussian slit function is expressed as



210

$$S(\lambda) = \frac{k}{2w\Gamma\left(\frac{1}{k}\right)} \exp\left[-\left|\frac{\Delta\lambda}{w}\right|^k\right], \quad (3)$$

211 where k is the shape factor and w is the slit width, with relative wavelength to band center wavelength,
 212 $\Delta\lambda$. This function can describe a wide variety of shapes just by varying k ; for $k=2$ it becomes the
 213 standard Gaussian and w represents the half width at $1/e$ intensity ($\text{FWHM} = 2\sqrt{\ln 2} w$). Compared
 214 to the standard Gaussian, the super Gaussian has broader peaks at the top and thinner wings if k is larger
 215 than 2 whereas it has sharper peaks and longer tails if k is smaller than 2. w of the super Gaussian
 216 function represents the half-width at $1/e^{\text{th}}$ intensity ($\text{FWHM} = 2\sqrt[k]{\ln 2}$). The symmetric or asymmetric
 217 standard Gaussian has been commonly assumed to derive OMI, GOME, and GOME-2 slit functions
 218 (Liu et al., 2005;2010; Nowlan et al., 2011; Cai et al., 2012; Munro et al., 2016). Recently the hybrid
 219 combination of standard and flat-top Gaussian functions has been implemented for characterizing OMI
 220 laboratory measurements of slit functions (Dirksen et al., 2006) and deriving airborne instrument slit
 221 functions (Liu et al., 2015a;2015b; Nowlan et al., 2016). The concept of this hybrid Gaussian function
 222 is very similar to the super Gaussian, but is a rather complex with more slit parameters. The super
 223 Gaussian function was introduced and tested as an analytical slit function by Beirle et al. (2017) and
 224 Sun et al. (2017a;b).

225 In general, the instrument line shape is assumed to be the same for both radiance and irradiance
 226 measurements from satellite observation and determined from irradiances due to lack of atmospheric
 227 interference. We simultaneously and iteratively determine the wavelength and slit calibration
 228 parameters through cross-correlation of the measured OMPS irradiances to simulated solar irradiances
 229 from a well calibrated, high-resolution solar irradiance reference spectrum (Chance and Kurucz, 2010).
 230 The simulation of solar irradiance, I_s is described as

$$231 \quad I_s(\lambda) = AI_o(\lambda + \Delta\lambda) \times \sum_{i=0}^2 P_i(\lambda - \lambda_{avg})^i, \quad (4)$$

232 where I_o is the convolved high-resolution solar reference spectrum with assumed slit functions, A is
 233 the scaling parameter for I_o . $\lambda + \Delta\lambda$ Indicates the process of wavelength calibration (e.g. shift and
 234 squeeze); only the wavelength shift is considered in this study. P_i represents the coefficients of a scaling
 235 polynomial (third order in this study). This approach was firstly introduced by Caspar and Chance
 236 (1997), and is widely used for wavelength and slit function calibrations in trace gas retrievals from
 237 UV/visible measurements.

238 In this experiment, the slit parameters, w and k or slit scaling are fitted from daily measured
 239 OMPS irradiances over the wavelength range 302-340 nm at each cross-track position. Note that this



240 slit calibration ignores the wavelength dependence for deriving analytic slit functions and slit scaling to
241 the measured slit functions; this is a good approximation based on Fig. 1b as the wavelength dependence
242 of the slit functions is small. But the variation of the slit shape with wavelength could be considered
243 with OMPS preflight measured slit functions given for every CCD dimension if it becomes necessary.
244 The left panels of Fig. 2 compare the derived slit parameters from OMPS irradiances using different
245 functions. The red line of Fig. 2.a.1 shows that a slight change of the preflight-measured slit functions
246 is required to model the OMPS irradiance measurements, by up to 4% at both edges. Therefore the
247 benefit of fitting measured slit functions over fixing them is found to be trivial ($\sim 0.001\%$) at nadir
248 cross-track pixels (12-30th); for edge pixels, the improvement in fitting residuals is more noticeable, up
249 to 0.18%. The shape factor (k) of the derived super Gaussian functions is found to be ~ 2.3 for left swath
250 and ~ 2.5 for right swath (Fig. 2.b.1), implying that they have broader peaks and thinner wings compared
251 to the standard Gaussian if slit widths are equal. The slit widths of three different slit functions show
252 similar variations with respect to cross-track positions. The FWHMs vary from widest at $\sim 12^{\text{th}}$ cross-
253 track position to narrowest at the edges, but they are significantly narrower at the rightmost cross-track
254 positions than at the leftmost ones. Compared to the standard Gaussian slit widths, the super Gaussian
255 slit widths show a much better agreement with measured slit widths; the average difference of slit widths
256 between measured and super (standard) Gaussian functions is ~ 0.01 (0.05) nm. In Fig. 3, an example
257 of the derived slit functions and fitted preflight slit functions shows that the shapes are very similar.

258 The wavelength calibrations using different slit functions are characterized for the ozone fitting
259 window and are shown in Fig. 4b. The shift parameter is determined from irradiance and radiance at
260 second cross-correlation step after slit parameters are determined from irradiances at first cross-
261 correlation step. Note that the wavelength shifts fitted between first and second steps are very similar,
262 indicating little correlation between slit and wavelength calibration parameters. This analysis indicates
263 that the accuracy of wavelength registration in level 1b data is on average 0.05 nm for earthshine
264 measurements and within 0.02 nm for solar measurements with consistent variation over all cross-track
265 pixels. However, the wavelength calibration results using OMPS measured slit functions show different
266 characteristics from those using both Gaussian-type slit functions, especially over left cross-track pixels.
267 The different wavelength shifts are likely because the original OMPS slit functions show slight
268 asymmetry and are used in the wavelength calibration of L1B data. There exists a ~ 0.05 nm shift
269 between irradiances and radiance. In ozone retrieval algorithm we shift neither radiance nor irradiance
270 to a reference spectra before retrievals, but the shift between irradiance and radiance is adjusted during
271 ozone retrievals to account for the on-orbit variations of wavelength shifts as mentioned in Sect. 2.3.



272 The right columns of Fig. 2 compare the impact of different slit functions on spectral fitting residuals
273 of solar irradiances, together with the average fitting residuals as a function of cross-track position in
274 Fig.4.a. Measured solar spectra are mostly within an average of ~ 1% of modeled solar spectra, except
275 for the first few wavelengths. Based on these fitting results, we revise the fitting window to 302.5-340
276 nm. The fitting residuals using a derived standard Gaussian function are the worst for all cross-track
277 positions. On the other hand, the super Gaussian slit function similarly represents the measured slit
278 function, but slightly improves the fitting accuracy at the 6~18 cross-track positions (Fig. 4.a). However,
279 the benefit of using the super Gaussian function for fitting OMPS radiances over the standard Gaussian
280 function is insignificant within 0.02 % (not shown here). These results agree well with Beirle et al.
281 (2017), who demonstrated the similar benefit of using Standard and Super Gaussian slit functions on
282 OMI and GOME-2 measurements. Moreover, the impact of using different slit functions could be less
283 important for OMPS than OMI and GOME-2 due to its coarser spectral resolution.

284 In summary, super Gaussian functions are recommended for the OMPS instrument slit functions
285 than the standard Gaussian functions if the on-orbit instrument slit functions largely deviate from the
286 preflight-measured slit functions due to instrument degradation or thermal-induced variation. In the rest
287 of this paper, the measured slit function is used for the analysis of OMPS measurements.

288

289 **3.2 Soft Calibration**

290 The OMPS instrument 2-D CCD detector array could be susceptible to artificial cross-track
291 dependent errors that are commonly seen in OMI trace gas retrievals. To eliminate this impact on the
292 OMI L2 product, soft calibration and post-processing cross-track smoothing have been typically
293 implemented: the first correction removes the systematic wavelength and cross-track dependent
294 component in measured radiances (Liu et al., 2010; Cai et al., 2012), whereas the second correction
295 removes cross-track dependent biases in retrievals (Kurosu et al., 2004; Hormann et al., 2016). Figure
296 5 compares our preliminary tropospheric and stratospheric ozone column retrievals with collocated
297 OMI retrievals on 14 March 2013. OMPS stratospheric retrievals show an excellent consistency with
298 OMI even though OMPS measurements does not cover much of the Hartley ozone absorption
299 wavelengths where most of the vertical information of stratospheric ozone comes from. This is because
300 the separation of stratospheric ozone columns from tropospheric ozone columns is still mainly
301 determined from wavelengths longer than 300 nm (Bak et al., 2013a). On the other hand, tropospheric
302 ozone retrievals are positively biased with respect to OMI, by amounts largely dependent on the OMI



303 cross-track position. Therefore, we decide to include a soft-calibration correction in our retrievals to
304 eliminate wavelength and cross-track dependent errors in OMPS radiances. A general approach to the
305 soft calibration is to characterize systematic differences between measured and computed radiances for
306 scenes where we could assume that all parameters are known; the tropics were typically selected since
307 ozone variability is relatively small (Liu et al., 2010). OMPS normalized radiances are simulated with
308 collocated OMI ozone profiles averaged and interpolated onto $5^\circ \times 5^\circ$ grid cells to fill in bad pixels
309 mostly caused by the row anomaly. Other forward model inputs are described in Sect. 2. We use 25 days
310 of data between 1 March 2013 and 25 March 2013 under the following conditions: latitude $< 15^\circ\text{N/S}$,
311 solar zenith angle (SZA) $< 40^\circ$, cloud fraction < 0.1 , and surface reflectivity < 0.1 . The systematic and
312 random components of measured-to-simulated radiance ratios are displayed in Fig. 6. Agreement is
313 mostly at the $\pm 2\%$ level below 310 nm, except at wavelengths shorter than ~ 302.5 nm where the
314 systematic biases increase sharply due to the overcorrection of straylight in OMPS v2.0 data processing.
315 For wavelengths longer than 310 nm, OMPS observations show negative biases with maximum of $\sim 3\%$
316 at 315 nm. The standard deviations of mean differences steadily increase from longer wavelengths to
317 302.5 nm (2–2.5%) and then sharply rise up to $\sim 4\%$. The abnormal features of fitting residuals below
318 302.5 nm shown in Figs. 2 and 6 provide a basis for why we select the lower boundary of the ozone
319 fitting window as 302.5 nm. The soft calibration is applied before the fitting starts by dividing OMPS
320 radiances by the derived correction spectrum just at the initial iteration with the assumption that the
321 systematic biases consistently exist independent of space and time. Figure 7 shows how our
322 tropospheric ozone retrievals are improved with our soft calibration in comparison with retrievals
323 shown in Fig. 5.b. The usefulness of our soft calibration implementation is also evaluated through
324 comparisons of the accuracies of the spectral fitting residuals with and without soft calibration as shown
325 in Fig. 8. The mean fitting residuals without soft calibration are $\sim \pm 1\%$ at shorter wavelengths < 320
326 nm for all latitudes and sky conditions, whereas for longer wavelengths they increase from 0.3 % to
327 0.5 % with increasing latitudes. Our soft calibration dramatically improves the fitting accuracy for both
328 clear and cloudy pixels, especially over the tropics and mid-latitude regions; fitting residuals are mostly
329 within 0.2 % at longer wavelengths > 310 nm. In high latitudes, improvements can be identified, but
330 large remaining systematic biases can still be found.

331 **3.3 Common Mode Correction**

332 In previous section, it is shown that our soft calibration effectively eliminates systematic biases of
333 measurements relative to VLIDORT simulations for most cases, except for high latitudes/SZAs where



334 there still exists a distinct wavelength-dependent pattern in fitting residuals because the soft calibration
335 spectrum is derived only under small SZA conditions. In order to verify and correct such systematic
336 biases remaining after soft calibration, we characterize spectral fitting residuals at the final iteration
337 classified into 3 latitude/SZA regimes (southern polar region/SZA>60°, tropical region/ SZA<40°,
338 northern polar region/ SZA>60°) for each cross-track position and for one day (14th or 15th) of each
339 month. The remainder is called the common residual spectrum. Examples of derived common spectra
340 are presented in Fig. 9 for March and August 2013. The main peak positions of residuals of all common
341 residual spectra are well matched to each other. The amplitude of tropical residuals is very similar
342 between two months, whereas the variation of the amplitude at high latitudes seems to be associated
343 with snow/ice cover and SZA variations such that the amplitude is maximized during the polar winter
344 season. Applying the common mode correction means subtracting the common spectrum with
345 amplitude determined iteratively along with the rest of state vector components from the measured
346 spectrum. Fig. 10 compares the fitting residuals at high SZAs for one orbit of data on 02 March 2013
347 with and without the common mode correction. It is evident that wavelength dependent fitting residuals
348 are greatly reduced even for the first few wavelengths, with amplitude of spectral residuals reduced
349 from ~ 1 % to 0.5 %. Moreover, the common mode correction slightly reduces the standard deviations
350 of residuals. The improvement is seen everywhere as shown in Fig. 11 where RMS of relative fitting
351 residuals (ratio of fitting residuals to measurements error) is displayed for all individual pixels within
352 one orbit.

353 **3.4 Measurement Error Correction**

354 The measurement error covariance matrix S_y is one of the essential inputs in an OE based algorithm,
355 because it significantly affects the stability of retrievals and retrieval sensitivities. OMPS L1B v2.0 data
356 contain the relative errors of radiance measurements, but these measurement errors (~ 0.04 % @ 320
357 nm) were too small to regularize our ozone fitting process so that many retrievals fail due to negative
358 or large positive ozone values as a result of over fitting. Ideally, the measurement errors need to include
359 not only photon shot noise but also other kinds of random noise errors caused by readout, straylight,
360 dark current, geophysical pseudo-random noise errors due to sub-pixel variability and motion when
361 taking a measurement, forward model parameter error (random part), and other unknown errors.
362 However, OMPS measurement errors reported in the L1B only include photon shot noise and read-out
363 errors, which underestimate the overall measurement error. For this reason, OMI floor noise errors
364 instead of OMPS random-noise errors are imposed on our preliminary retrievals, as mentioned in Sect



365 2.3. However, better signal-to-noise ratios (SNRs) could be expected for OMPS than OMI due to
366 OMPS's coarser spectral and spatial resolutions, as shown from the improved detection limit of OMPS
367 H₂CO retrievals compared to OMI as discussed in Gonzalez Abad et al. (2016). Fig. 11 also implies that
368 there is room for increasing the Degrees of Freedom for Signals (DFS) to current ozone retrievals by
369 regularizing them using the improved measurement error instead of using OMI floor noise error; the
370 ideal value of RMS is one, but our RMS is mostly within 0.4 at low and mid-latitudes. The random-
371 noise component of measurements could be derived from standard deviations of spectral fitting
372 residuals (Cai et al., 2012; Liu et al. 2015b). Fig. 12 shows how we derive the measurement errors to
373 improve our retrievals. We first characterize the minimum measurement errors from fitting residuals
374 under nearly clear-sky condition at SZAs < 40° and cross-track pixels between 4 and 33; note that no
375 radiometric calibration is applied to these fitting residuals. The standard deviations of fitting residuals
376 are nearly invariant at longer wavelengths > 310 nm and show a significant increase from ~ 0.1 % at
377 310 nm to ~ 0.3 % at 302 nm as plotted with the red dashed line in Fig. 12.a. We eliminate the low-
378 frequency portion of the noises with a 4th order polynomial fit to define the minimum OMPS floor noise
379 (FN) errors as plotted with the red solid line in Fig. 12.a. The derived FN errors are ~ 2 (1.5-4) times
380 smaller than OMI floor noise errors above (below) 310 nm and thereby could increase the measurement
381 information in our retrievals. We impose the minimum FN errors as a measurement constraint in our
382 algorithm when SZAs are smaller than ~ 20°, whereas they are multiplied by a SNR scaling factor to
383 increase measurement errors as a function of SZAs. Figure 12.b shows an example of how derived
384 measurement errors increase with SZA at the boundary wavelengths of the ozone fitting window, with
385 errors from 0.24 % to 0.45 % for 302.5 nm and from 0.097 % to 0.19 % for 340 nm.

386 Figure 13 shows the effect of using the derived FN errors on our retrievals. The RMS of fitting
387 residuals increases from 0.2-0.4 to 0.4-0.8 in swath lines 50-350, where SZAs are within ~ 60°, due to
388 SNR increases, whereas the average fitting residuals slightly improves by 0.015 %. Using the new FN
389 errors slightly increases the number of iterations; one or more iterations are required for ~ 24 % of the
390 total retrieved pixels and hence our fitting process converges mostly within 3-4 times, except for thick
391 clouds where the number of iterations increases to 6. Using the derived FN errors significantly increases
392 the retrieval information content. Both stratospheric and tropospheric DFSs are improved by 0.2-0.4
393 under mild SZAs and by up to 0.2 under high SZAs as shown in Fig. 14, so that tropospheric ozone
394 retrievals demonstrate ~ 1 DFS in low/mid latitudes, which is similar to OMI retrievals (Liu et al.,
395 2010a). Fig 15.a shows the retrieved tropospheric ozone column distribution with two radiometric
396 calibrations (soft, CMC) and OMPS FN errors. Compared to Fig 7.b without CMC and OMI FN errors,
397 the cross-track dependent noises over the polar region are smoothed due to CMC and the columns are



398 enhanced in the tropics and the northern mid-latitudes due to OMPS FN errors. Successful tropospheric
399 retrievals typically require better than 0.2-0.3 % fitting accuracy between measured and modeled
400 radiances in the Huggins band (310-340 nm) (Munro et al., 1998). Our fitting algorithm meets this
401 requirement after carefully applying empirical calibrations as shown in Fig 15.b; the average fitting
402 residuals are within 0.1 % for moderate SZAs, with insignificant dependence on cross-track position.

403 **4. Conclusions**

404 The OMI ozone profile algorithm has been adapted and modified to retrieve tropospheric ozone and
405 ozone profiles from OMPS-NM L1B 2.0 product. To verify the best knowledge of OMPS instrument
406 slit functions, we evaluate OMPS preflight measured slit functions and analytical slit functions
407 assuming standard and super Gaussian distributions through cross-correlation using a high-resolution
408 solar reference spectrum. We also adjust preflight measured slit functions to post-launch OMPS
409 measurements by broadening/squeezing them by up to 4%, which slightly improves the fitting residuals
410 at nadir cross-track pixels, but by up to 0.18% (e.g., from 0.75% to 0.6% at the first cross-track position)
411 at edge pixels. The super Gaussian slit functions better represent OMPS irradiances than the standard
412 Gaussian and even the preflight measured slit functions, but the fitting residuals of radiances with
413 different slit functions show insignificant differences. OMPS measured slit functions are finally
414 implemented in our OMPS ozone fitting retrievals because they take account of the slight dependence
415 of slit functions on wavelengths.

416 We perform two kinds of radiometric calibrations to eliminate the systematic components of fitting
417 residuals. First, we apply “soft calibration” to OMPS radiance before retrievals. This correction
418 spectrum is derived as a function of wavelength and cross-track position by averaging the ratio of
419 measured radiances to simulated radiances using collocated OMI ozone profile retrievals in the tropics
420 under nearly clear-sky conditions for 25 days of May 2013. Applying soft calibration to OMPS radiance
421 dramatically improves the spectral fitting residuals, especially under low to moderate SZA. The
422 amplitude of fitting residuals decreases from 1 % to 0.2 %. Therefore, the significant cross-track striping
423 pattern shown in preliminary OMPS tropospheric ozone retrievals is mostly eliminated. Second, the
424 CMC is implemented to compensate fitting residuals uncorrected by soft calibration, especially for high
425 SZA retrievals. This correction spectrum is derived as functions of wavelength and cross-track position
426 by averaging one day’s fitting residuals over the tropics and northern/southern high latitude regions,
427 respectively. The amplitude of the correction spectrum is iteratively and simultaneously adjusted with



428 ozone. It is found that the amplitude of the fitting residuals decreases by a factor of 2 due to the CMC
429 over high latitudes.

430 Our preliminary algorithm uses OMI floor noise errors to represent measurement constraints because
431 OMPS L1B random-noise errors are too tight to stabilize retrievals. However, we found that OMI floor
432 noise errors cannot sufficiently constrain our OMPS retrievals, indicating that there is room to increase
433 the retrieval sensitivity to measurement information by improving measurement constraints. Therefore,
434 we derive the minimum floor noise (FN) error corresponding to standard deviations of spectral fitting
435 residuals over the tropics. The derived minimum FN error is $\sim 0.097\%$ in 310-340 nm and increases to
436 $\sim 0.24\%$ at 302.5 nm, which is smaller than OMI error by a factor of 1.5-4 below 310 nm and 2 above.
437 We apply this OMPS FN error at SZAs $< \sim 20^\circ$ and those multiplied by a SNR scaling factor to take
438 into account the decreasing SNR with increasing SZA at SZAs $> \sim 20^\circ$; at SZA = 90° errors becomes
439 0.45 % at 302.5 nm and 0.19 % at 340 nm. Using OMPS FN errors as a retrieval constraint slightly
440 improves the fitting residuals, by 0.015 % on average, and both stratospheric and tropospheric ozone
441 retrieval sensitivity (DFS increases by 0.2-0.4), but requires 1 or more additional iterations for
442 convergence. In this study, we meet the requirement to achieve successful tropospheric ozone retrievals
443 in terms of DFS (> 1) and fitting residuals (< 0.2 - 0.3%) with empirical calibrations optimized to OMPS
444 L1B measurements. In future work, we will characterize OMPS ozone profile retrievals, present error
445 analysis, and validate retrievals using a reference dataset, to verify that the quality of OMPS ozone
446 retrievals is adequate for scientific use.

447

448 **Acknowledgements**

449 We acknowledge the OMI and OMPS science teams for providing their satellite data and Glen Jaross
450 for providing useful comments regarding OMPS level 1B v2.0 data. We thank Alexander Vasilkov for
451 allowing the OMPS cloud product to be used in this study. Research at Pusan National University by J.
452 Bak and J.H. Kim was financially supported by the 2016 Post-Doc. Development Program of Pusan
453 National University. Research at the Smithsonian Astrophysical Observatory by X. Liu, K. Chance, and
454 K. Sun was funded by NASA Aura science team program (NNX14AF16G) and the Smithsonian
455 Institution. K. Yang was funded by NASA Suomi NPP science team program (NNX14AR20A).

456 **References**

- 457 Bak, J., Kim, J. H., Liu, X., Chance, K., and Kim, J.: Evaluation of ozone profile and tropospheric ozone
458 retrievals from GEMS and OMI spectra, *Atmos. Meas. Tech.*, 6, 239–249, doi:10.5194/amt-6-239-
459 2013, 2013a.
- 460 Bak, J., Libaku, X., Wei, J. C., Pan, L. L., Chance, K., and Kim, J. H.: Improvement of OMI ozone
461 profile retrievals in the upper troposphere and lower stratosphere by the use of a tropopause-based
462 ozone profile climatology, *Atmos. Meas. Tech.*, 6, 2239–2254, doi:10.5194/amt-6-2239-2013,
463 2013b.
- 464 Beirle, S., Lampel, J., Lerot, C., Sihler, H., and Wagner, T.: Parameterizing the instrumental spectral
465 response function and its changes by a super-Gaussian and its derivatives, *Atmos. Meas. Tech.*, 10,
466 581–598, <https://doi.org/10.5194/amt-10-581-2017>, 2017.
- 467 Bhartia, P. K. and Wellemeyer, C.: TOMS-V8 total O3 algorithm, in: OMI Algorithm Theoretical Basis
468 Document, Vol. II, OMI Ozone Products, edited by: Bhartia, P. K., 15–31, NASA Goddard Space
469 Flight Cent., Greenbelt, MD, 2002.
- 470 Bovensmann, H., Burrows, J. P., Buchwitz, M., Frerick, J., Noel, S., Rozanov, V. V., Chance, K. V.,
471 and Goede, A. P. H.: SCIAMACHY: Mission objectives and measurement modes, *J. Atmos. Sci.*,
472 56, 127–150, doi:10.1175/1520-0469(1999)056<0127:SMOAMM>2.0.CO;2, 1999.
- 473 Brion, J., Chakir, A., Daumont, D., and Malicet, J.: High-resolution laboratory absorption cross section
474 of O3. Temperature effect, *Chem. Phys. Lett.*, 213, 610–612, 1993.
- 475 Cai, Z., Liu, Y., Liu, X., Chance, K., Nowlan, C. R., Lang, R., Munro, R., and Suleiman, R.: ,
476 Characterization and correction of Global Ozone Monitoring Experiment 2 ultraviolet
477 measurements and application to ozone profile retrievals, *J. Geophys. Res.*, 117, D07305,
478 doi:10.1029/2011JD017096, 2012.
- 479 Caspar, C. and Chance, K.: GOME wavelength calibration using solar and atmospheric spectra, Third
480 ERS Symposium on Space at the Service of our Environment, Florence, Italy, 14–21 March, 1997.
- 481 Chance, K. and Kurucz, R. L.: An improved high-resolution solar reference spectrum for earth's
482 atmosphere measurements in the ultraviolet, visible, and near infrared, *J. Quant. Spectrosc. Ra.*,
483 111, 1289–1295, doi:10.1016/j.jqsrt.2010.01.036, 2010.
- 484 Chance, K., Liu, X., Suleiman, R. M., Flittner, D. E., Al-Saadi, J., and Janz, S. J.: Tropospheric
485 emissions: monitoring of pollution (TEMPO), *Proc. SPIE 8866, Earth Observing Systems XVIII*,
486 8866, 88660D-1–88660D-16, doi:10.1117/12.2024479, 2013.
- 487 Dirksen, R., Dobber, M., Voors, R., and Levelt, P.: Prelaunch characterization of the Ozone Monitoring
488 Instrument transfer function in the spectral domain, *Appl. Opt.*, 45, 3972–3981,
489 10.1364/ao.45.003972, 2006.
- 490 European Space Agency: The GOME Users Manual, ESA Publ. SP-1182, Publ. Div., Eur. 488 Space
491 Res. and Technol. Cent., Noordwijk, The Netherlands, 1995.



- 492 European Organisation for the Exploitation of Meteorological Satellites (EUMETSAT) : GOME-2 level
493 1 Product Generation Specification, Rep. EPS.SYS.SPE.990011, Darmstadt, Germany, 2006.
- 494 Flynn, L., Long, C., Wu, X., Evans, R., Beck, C. T., Petropavlovskikh, I., McConville, G., Yu, W.,
495 Zhang, Z., Niu, J., Beach, E., Hao, Y., Pan, C., Sen, B., Novicki, M., Zhou, S., and Seftor, C. :
496 Performance of the Ozone Mapping and Profiler Suite (OMPS) products, *J. Geophys. Res. Atmos.*,
497 119, 6181–6195, doi:10.1002/2013JD020467, 2014.
- 498 G. González Abad, A. Vasilkov, C. Seftor, X. Liu, and K. Chance: Smithsonian Astrophysical
499 Observatory Ozone Mapping and Profiler Suite (SAO OMPS) formaldehyde retrieval, *Atmos.*
500 *Meas. Tech.*, 9, 2797-2812, 2016.
- 501 Huang, G., Liu, X., Chance, K., Yang, K. et al.: Validation of 10-year SAO OMI Ozone Profile
502 (PROFOZ) Product Using Ozonesonde Observations, *Atmos. Meas. Tech. Discuss.*,
503 doi:10.5194/amt-2017-15, 2017.
- 504 Hörmann, C., Sihler, H., Beirle, S., Penning de Vries, M., Platt, U., and Wagner, T.: Seasonal variation
505 of tropospheric bromine monoxide over the Rann of Kutch salt marsh seen from space, *Atmos.*
506 *Chem. Phys.*, 16, 13015-13034, doi:10.5194/acp-16-13015-2016, 2016.
- 507 Jaross, G.: OMPS/NPP L1B NM Radiance EV Calibrated Geolocated Swath Orbital V2, Goddard Earth
508 Sciences Data and Information Services Center (GES DISC), Greenbelt, MD, USA, accessed July
509 20, 2017, doi:10.5067/DL081SQY7C89, 2017
- 510 Kleipool, Q. L., Dobber, M. R., de Haan, J. F., and Levelt, P. F.: Earth surface reflectance climatology
511 from 3 years of OMI data, *J. Geophys. Res.*, 113, D18308, doi: 10.1029/2008JD010290, 2008.
- 512 Kroon, M., de Haan, J. F., Veefkind, J. P., Froidevaux, L., Wang, R., Kivi, R., and Hakkarainen, J. J.:
513 Validation of operational ozone profiles from the Ozone Monitoring Instrument, *J. Geophys. Res.*,
514 116, D18305, doi: 10.1029/2010JD015100, 2011.
- 515 Kurosu, T.P., Chance, K., and Sioris, C.E. : "Preliminary results for HCHO and BrO from the EOS-
516 Aura Ozone Monitoring Instrument", in *Passive Optical Remote Sensing of the Atmosphere and*
517 *Clouds IV*, Proc. of SPIE Vol. 5652 , doi: 10.1117/12.578606, 2004.
- 518 Levelt, P. F., van den Oord, G. H. J., Dobber, M. R., Malkki, A., Visser, H., de Vries, J., Stammes, P.,
519 Lundell, J. O. V., and Saari, H.: The Ozone Monitoring Instrument, *IEEE Trans. Geosci. Remote*
520 *Sens.*, 44(5), 1093–1101, doi:10.1109/TGRS.2006.872333, 2006.
- 521 Liu, X., Chance, K., Sioris, C. E., Spurr, R. J. D., Kurosu, T. P., Martin, R. V., and Newchurch, M. J.:
522 Ozone profile and tropospheric ozone retrievals from Global Ozone Monitoring Experiment:
523 algorithm description and validation, *J. Geophys. Res.*, 110, D20307, doi: 10.1029/2005JD006240,
524 2005.
- 525 Liu, X., Chance, K., Sioris, C.E, and Kurosu, T.P: Impact of using different ozone cross sections on
526 ozone profile retrievals from GOME ultraviolet measurements. *Atmos. Chem. Phys.*, 7, 3571-3578,
527 2007.



- 528 Liu, X., Bhartia, P.K, Chance, K, Spurr, R.J.D., and Kurosu, T.P.: Ozone profile retrievals from the
529 ozone monitoring instrument. *Atmos. Chem. Phys.*, 10, 2521–2537, 2010a.
- 530 Liu, C., Liu, X., Kowalewski, M.G., Janz, S.J., González Abad, G., Pickering, K.E., Chance, K., and
531 Lamsal, L.N.: Characterization and verification of ACAM slit functions for trace gas retrievals
532 during the 2011 DISCOVER-AQ flight campaign, *Atmos. Meas. Tech.*, 8, 751-759,
533 doi:10.5194/amt-8-751-2015, 2015a.
- 534 Liu, C., Liu, X., Kowalewski, M.G., Janz, S.J., González Abad, G., Pickering, K.E., Chance, K., and
535 Lamsal, L.N.: Analysis of ACAM Data for Trace Gas Retrievals during the 2011 DISCOVER-AQ
536 Campaign, *J. Spectroscopy*, ID827160, doi:10.1155/2015/827160, 2015, 827160, 2015b.
- 537 Munro, R., Lang, R., Klaes, D., Poli, G., Retscher, C., Lindstrot, R., Huckle, R., Lacan, A., Grzegorski,
538 M., Holdak, A., Kokhanovsky, A., Livschitz, J., and Eisinger, M.: The GOME-2 instrument on the
539 MetOp series of satellites: instrument design, calibration, and level 1 data processing – an overview,
540 *Atmos. Meas. Tech.*, 9, 1279-1301, doi:10.5194/amt-9-1279-2016, 2016.
- 541 Nowlan, C. R., Liu, X., Chance, K., Cai, Z., Kurosu, T. P., Lee, C., and Martin, R. V.: Retrievals of
542 sulfur dioxide from the global ozone monitoring experiment 2 (GOME-2) using an optimal
543 estimation approach: algorithm and initial validation, *J. Geophys. Res.-Atmos.*, 116, D18301,
544 doi:10.1029/2011JD015808, 2011.
- 545 Rodgers, C. D.: *Inverse Methods for Atmospheric Sounding: Theory and Practice*, World Scientific
546 Publishing, Singapore, 2000.
- 547 Pittman, J.V., Pan, L.L., Wei, J.C., Irion, F.W., Liu, X., Maddy, E.S., Barnet, C.D., Chance, K., and
548 Gao, R.-S.: Evaluation of AIRS, IASI, and OMI ozone profile retrievals in the extratropical
549 tropopause region using in situ aircraft measurements, *J. Geophys. Res.*, 114, D24109,
550 doi:10.1029/2009JD012493, 2009.
- 551 Schenkeveld, V. M. E., Jaross, G., Marchenko, S., Haffner, D., Kleipool, Q. L., Rozemeijer, N. C.,
552 Veefkind, J. P., and Levelt, P. F.: In-flight performance of the Ozone Monitoring Instrument,
553 *Atmos. Meas. Tech.*, 10, 1957-1986, <https://doi.org/10.5194/amt-10-1957-2017>, 2017.
- 554
- 555 Seftor, C. J., Jaross, G., Kowitt, M., Haken, M., Li, J., and Flynn, L. E.: Postlaunch performance of the
556 Suomi National Polar orbiting Partnership Ozone Mapping and Profiler Suite (OMPS) nadir
557 sensors, *J. Geophys. Res. Atmos.*, 119, doi: 10.1002/2013JD020472., 2014.
- 558 Seftor, C. J. and Jaross, G.: NMEV-L1B Data Release Notes,
559 https://ozoneaq.gsfc.nasa.gov/omps/media/docs/NMEV-L1B_Release_Notes.pdf, accessed 20 July
560 2017.
- 561
- 562 Sioris, C. E., and Evans, W. F. J.: Impact of rotational Raman scattering in the O₂ A band, *Geophys.*
563 *Res. Lett.*, 27(24), 4085–4088, 2000.



- 564 Spurr, R. J.: VLIDORT: A linearized pseudo-spherical vector discrete ordinate radiative transfer code
565 for forward model and retrieval studies in multilayer multiple scattering media, *J. Quant. Spectrosc.*
566 *Ra.*, 102, 316–342, doi:10.1016/j.jqsrt.2006.05.005, 2006.
- 567 Spurr, R. J. D.: Linearized pseudo-spherical scalar and vector discrete ordinate radiative transfer models
568 for use in remote sensing retrieval problems, in: *Light Scattering Reviews*, edited by: Kokhanovsky,
569 A., Springer, New York, 2008.
- 570 Sun, K., Liu, X., Huang, G., González Abad, G., Cai, Z., Chance, K., and Yang, K.: Deriving the slit
571 functions from OMI solar observations and its implications for ozone-profile retrieval, *Atmos.*
572 *Meas. Tech. Discuss.*, <https://doi.org/10.5194/amt-2017-129>, in review, 2017.
- 573 Sun, K., Liu, X., Huang, G., González Abad, G., Cai, Z., Chance, K., and Yang, K.: Deriving the slit
574 functions from OMI solar observations and its implications for ozone-profile retrieval, *Atmos.*
575 *Meas. Tech. Discuss.*, <https://doi.org/10.5194/amt-2017-129>, in review, 2017.
- 576 Vasilkov, A., Joiner, J., and Seftor, C.: First results from a rotational Raman scattering cloud algorithm
577 applied to the Suomi National Polar-orbiting Partnership (NPP) Ozone Mapping and Profiler Suite
578 (OMPS) Nadir Mapper, *Atmos. Meas. Tech.*, 7, 2897–2906, doi: 10.5194/amt-7-2897-2014, 2014.
- 579 Veefkind, J. P., Aben, I., McMullan, K., Förster, H., de Vries, J., Otter, G., Claas, J., Eskes, H. J., de
580 Haan, J. F., Kleipool, Q., van Weele, M., Hasekamp, O., Hoogeveen, R., Landgraf, J., Snel, R., Tol,
581 P., Ingmann, P., Voors, R., Kruizinga, B., Vink, R., Visser, H. and Levelt, P. F.: TROPOMI on the
582 ESA Sentinel-5 Precursor: A GMES mission for global observations of the atmospheric
583 composition for climate, air quality and ozone layer applications, *Remote Sensing of Environment*,
584 120(0), 70–83, doi:10.1016/j.rse.2011.09.027, 2012.
- 585 Yang, K., Dickerson, R.R., Carn, S.A., Ge, C., and Wang, J.: First observations of SO₂ from the
586 satellite Suomi NPP OMPS: Widespread air pollution events over China, *GRL.*,
587 doi:10.1002/grl.50952, 2013.
- 588 Yang, K., Carn, S. A., Ge, C., Wang, J., and Dickerson, R. R.: Advancing measurements of tropospheric
589 NO₂ from space: New algorithm and first global results from OMPS, *Geophys. Res. Lett.*, 41, doi:
590 10.1002/2014GL060136, 2014.
- 591 Zoogman, P. et al.: Tropospheric Emission: Monitoring of Pollution (TEMPO), *J. Quant. Spectrosc. &*
592 *Radiat. Transfer*, 186, 17–39, doi:org/10.1016/j.jqsrt.2016.05.008, 2017.
- 593
594
595
596
597
598
599



600

601 **Table 1. Surface and atmospheric input parameters and cross section data used in forward model**
602 **calculations.**

Forward model Parameters	Data Source
O ₃ cross sections	Brion et al. (1993)
Ozone Profile ^a	OMI ozone profiles from Liu et al. (2010)
Temperature profile, surface/tropopause pressure	Daily National Centers for Environmental Prediction (NCEP) final (FNL) operational global analysis data (http://rda.ucar.edu/datasets/ds083.2/)
Surface albedo	OMI surface climatology (Kleipool et al., 2008)
Cloud fraction	Derived at 347 nm
Cloud-top pressure ^b	OMPS Cloud Optical Centroid Pressures (OCPs) (Vasilkov et al., 2014)

603 ^aOMI ozone profiles retrieved at 48×52 km² with spatial coadding and then interpolated to 5° × 5° to fill
604 bad pixels.

605 ^bOCPs retrieved from OMPS-NM L1B v1.0 measurements using a rotational Raman scattering cloud
606 algorithm.

607

608

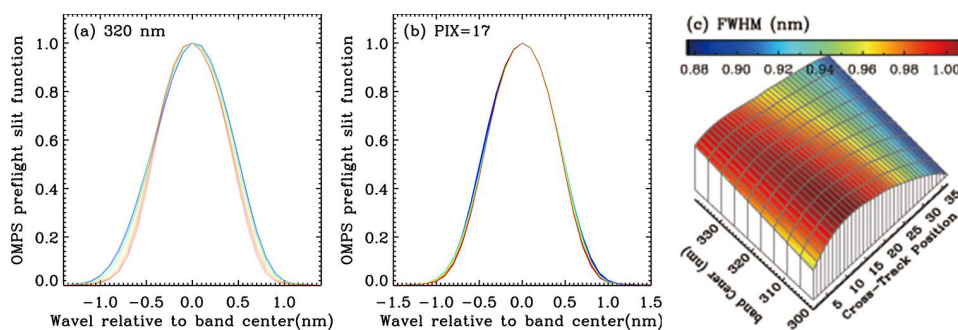
609

610

611

612

613



614

615 **Figure 1. (a) OMPS preflight slit function at 320 nm band center, with colors representing different cross-**
 616 **track positions from 1 (blue) to 36 (red). (b) Same as (a), but for the 17th cross-track position, with colors**
 617 **representing different wavelengths from 300 nm (blue) to 340 nm (red). (c) Full Width at Half Maximum**
 618 **(FWHM) in nm as functions of cross-track positions (x-axis) and band center wavelengths (y-axis) ranging**
 619 **from 300 to 340 nm.**

620

621

622

623

624

625

626

627

628

629

630

631

632

633

634

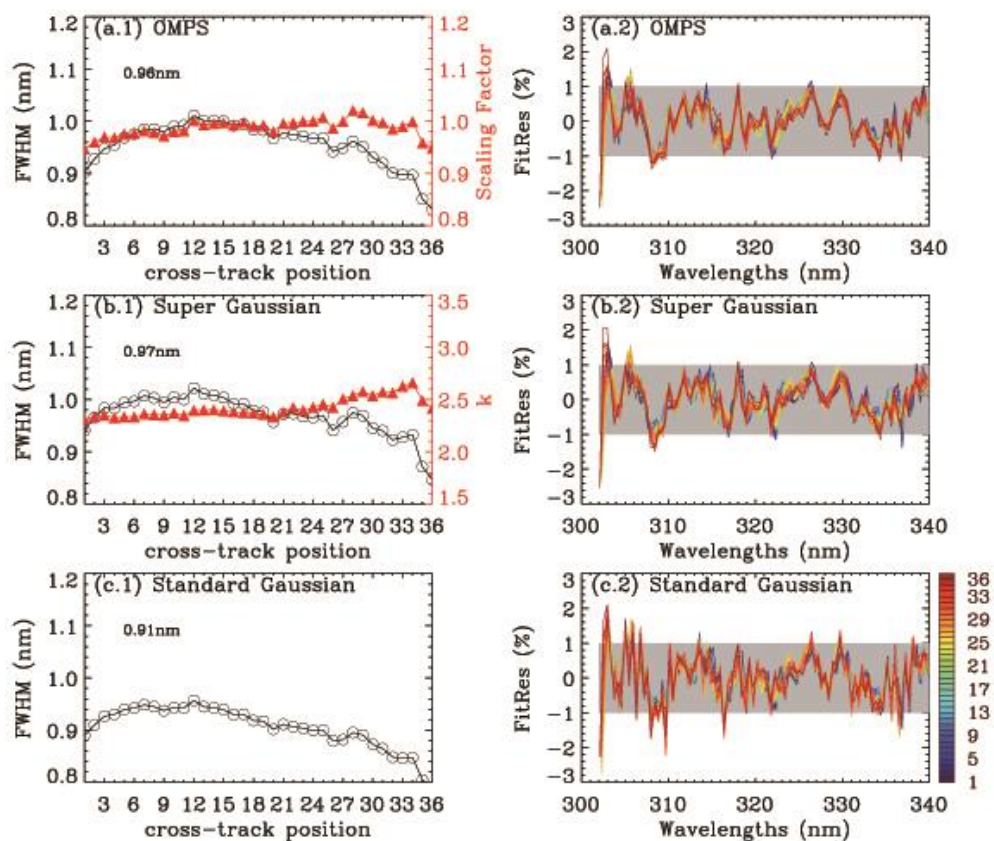
635

636

637



638



639

640 Figure 2. (Left) Slit function parameters as a function of cross-track position (1th-36th) for three different
 641 slit functions from OMPS irradiance measurements (302-340 nm) for orbit 7132 on 14 March 2013. The
 642 legends represent the FWHM averaged over all spectral pixels. (Right) The corresponding relative fitting
 643 residuals between measured and simulated irradiance spectra.

644

645

646

647

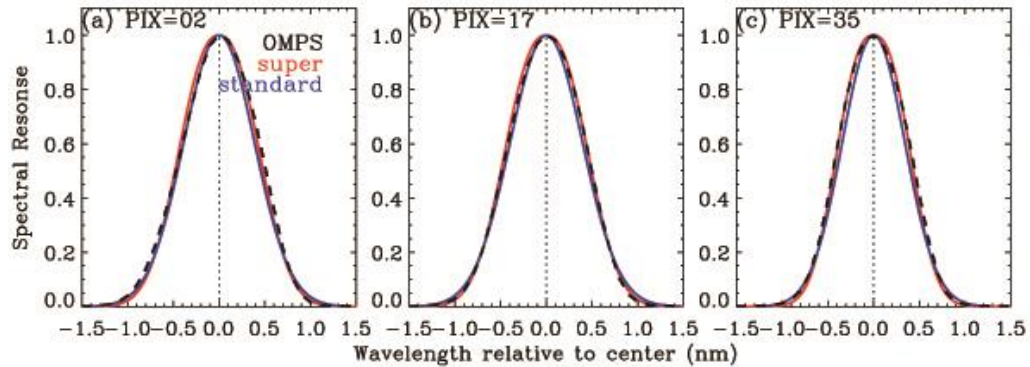
648

649

650



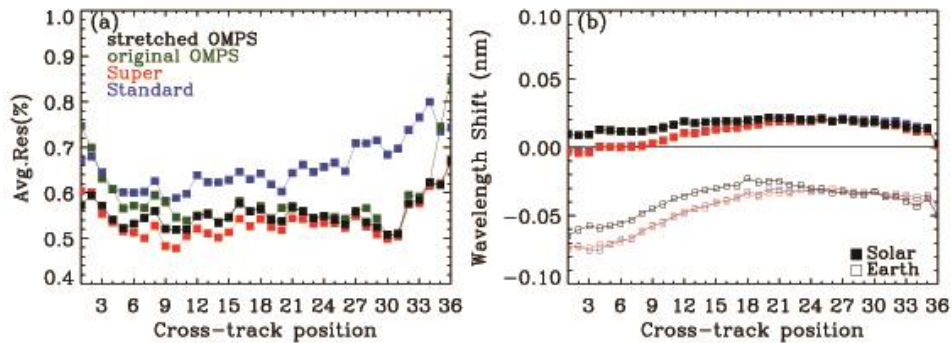
651



652

653 **Figure 3.** Comparison of OMPS measured slit measurements (black) and derived slit functions assuming a
 654 standard Gaussian (red) and super Gaussian (blue) for orbit 7132.

655



656

657 **Figure 4.** Same as Fig. 2, but for (a) average fitting residuals (%) as a function of cross-track positions. The
 658 green line represents the fitting residuals with measured OMPS slit functions without fitting a scaling factor.
 659 (b) Wavelength shifts between OMPS irradiance and reference spectrum (filled symbols) and between
 660 OMPS radiance at the middle swath line and reference spectrum (opened symbols).

661

662

663

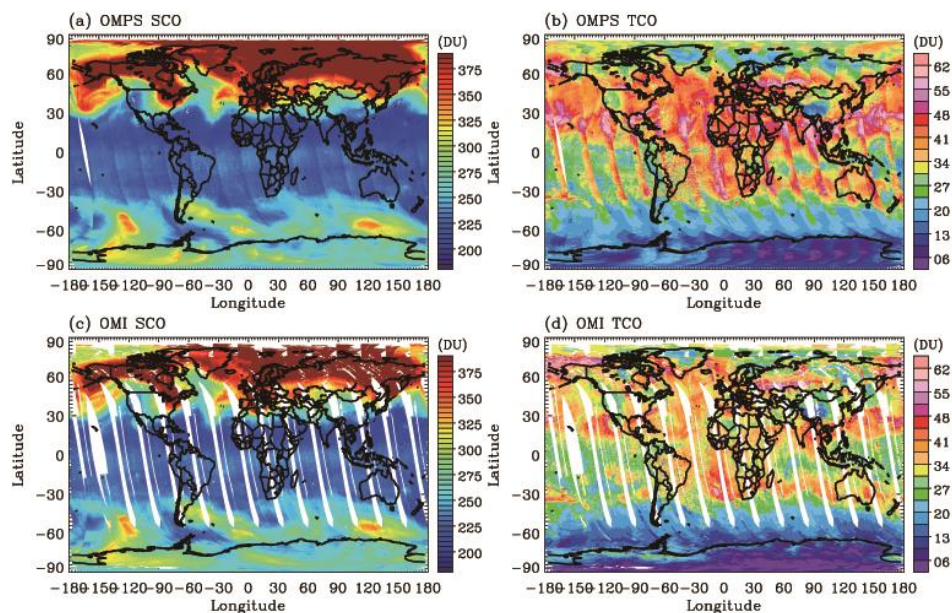
664

665



666

667



668

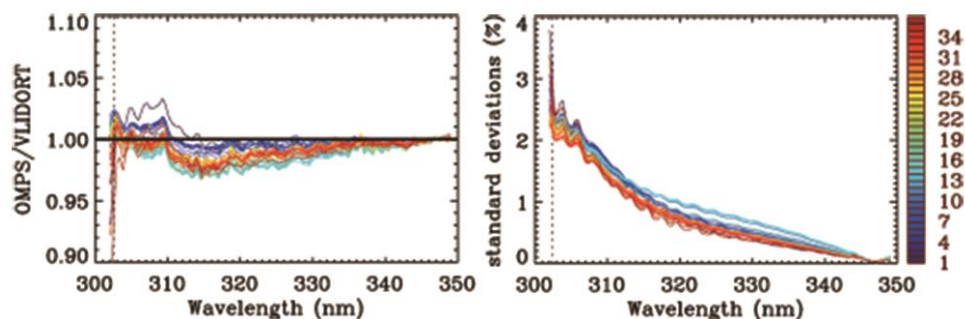
669 **Figure 5. Maps of stratospheric and tropospheric ozone column on 14 March 2013, retrieved from OMPS**
670 **(top) without any correction and OMI (bottom) measurements, respectively.**

671

672

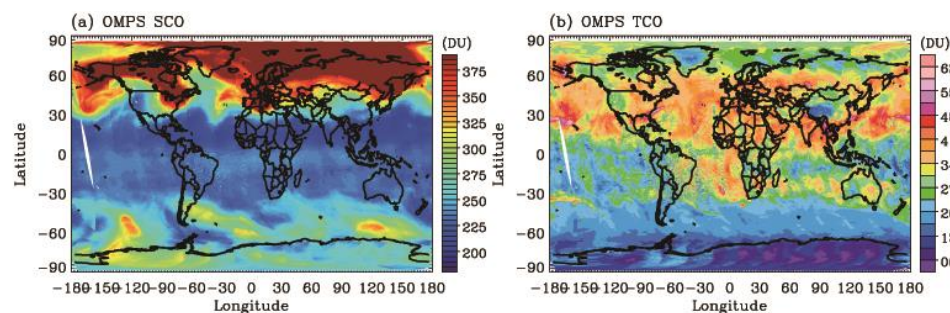
673

674



675

676 **Figure 6. (a)** Soft calibration spectrum derived from OMPS measured to simulated radiance ratio at initial
677 iteration, as a function of wavelength ranging from 302 nm to 350 nm. The vertical dotted line indicates
678 302.5 nm. OMPS data used in this calculation is limited to tropical clear-sky conditions (latitude $< \pm 15^\circ$,
679 cloud fraction < 0.1 , surface reflectivity < 0.1) for 25 days between 1 March 2013 and 25 March 2013.
680 Forward model inputs listed in Table 1 are used for OMPS simulations. **(b)** Standard deviations of fitting
681 residuals. Different colors represent various cross-track positions.



682

683 **Figure 7. Same as Figure 5 (a) and (b), but for OMPS ozone retrievals with soft calibration.**

684

685

686

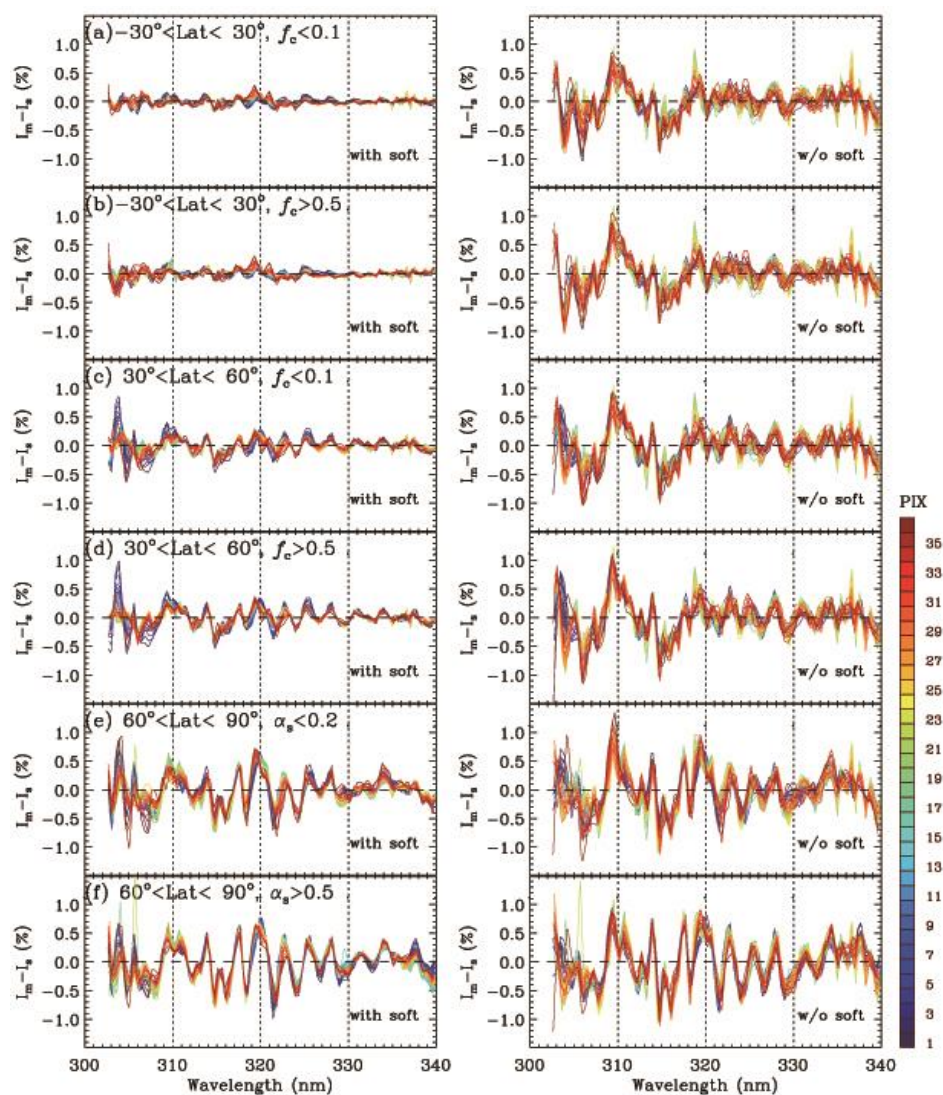
687

688

689

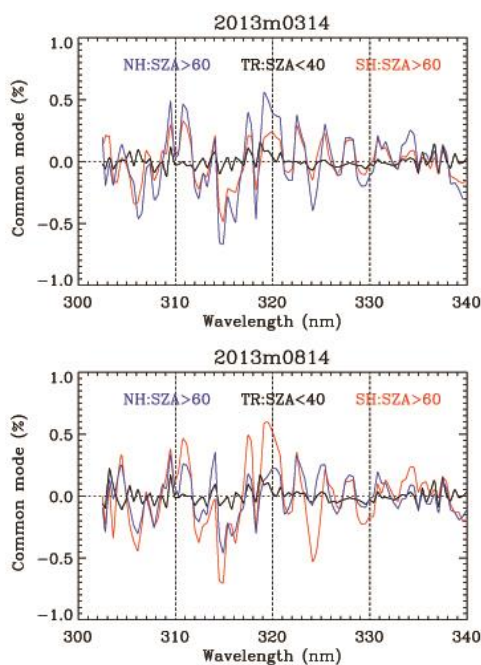
690

691



692

693 **Figure 8.** Comparison of fitting residuals on 14 March 2013 with (left) and without (right) soft calibration
 694 for 6 cases: (a-b) Tropics and (c-d) mid-latitudes each for clear sky (effective cloud fraction, $f_c < 0.1$) and
 695 cloudy ($f_c > 0.5$) conditions and (e-f) high-latitudes for snow-free and snow-covered surface conditions.
 696 Different colors represent different cross-track positions.



697

698 **Figure 9. Common mode spectra derived from final fitting residuals at the 17th cross-track position using**
699 **one day of measurements in March (upper) and August (lower), respectively. Note that tropical residuals**
700 **are derived from nearly clear-sky conditions where SZA < 40°, cloud fraction < 0.1, and surface albedo <**
701 **0.1. No special data screening is applied for polar residual spectra, except for SZA > 60°.**

702

703

704

705

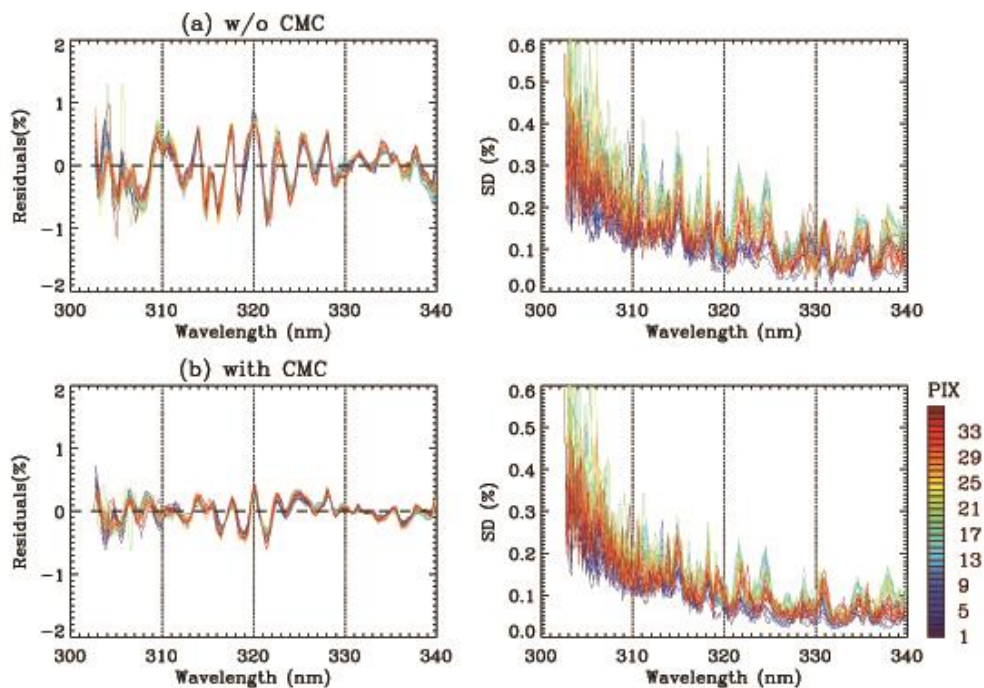
706

707

708

709

710

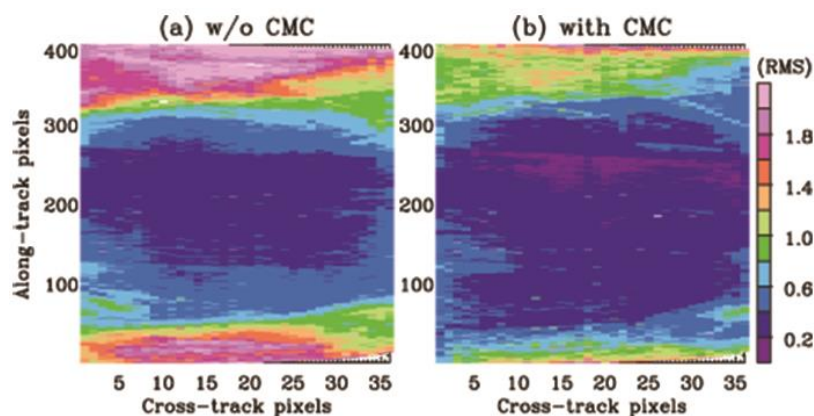


711
712 **Figure 10. Comparisons of mean fitting residuals (%) and its standard deviations (%) for latitude > 60°,**
713 **with different cross-track positions in different colors for one orbit data (6962) on 02 March 2013, without**
714 **(a) and with (b) common residual correction.**

715

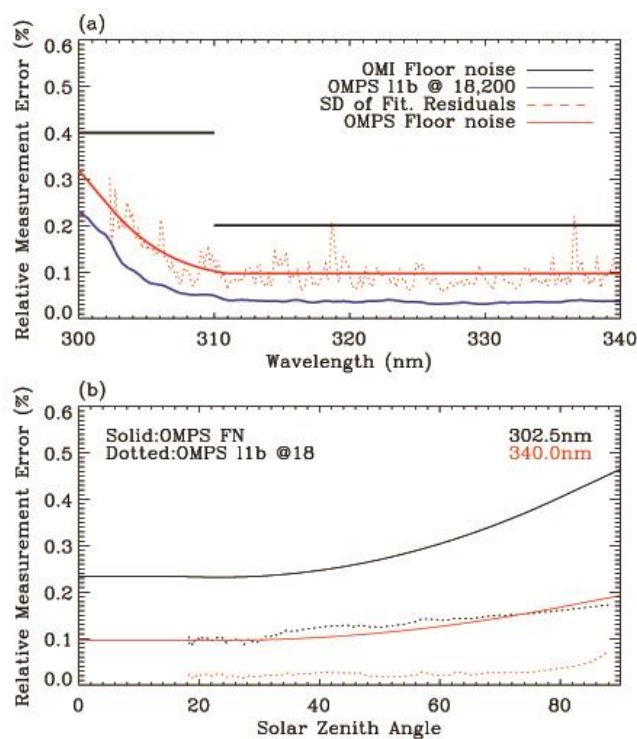
716

717



718

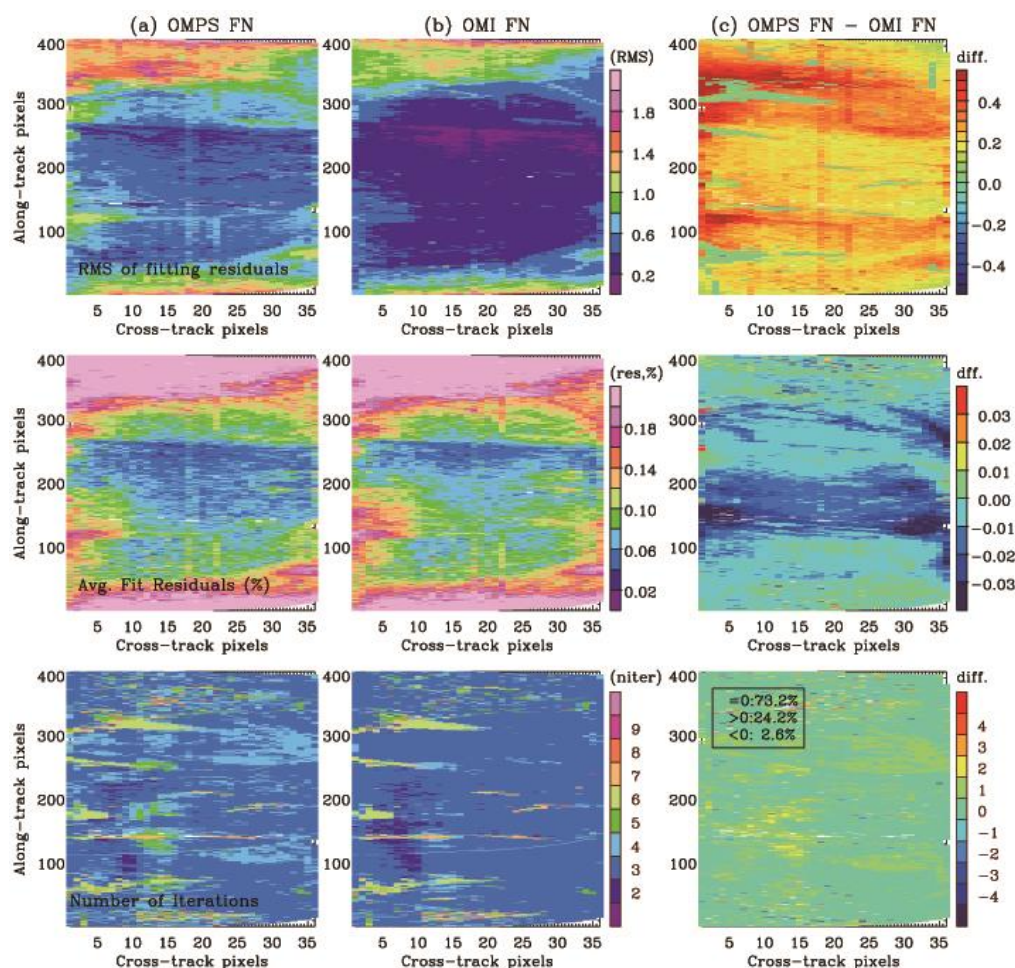
719 Figure 11. Same as Figure 10, but for Root Mean Square (RMS) of fitting residuals relative to the
720 measurement errors as functions of along- and cross-track pixels. The RMS is defined as $\sqrt{\frac{1}{n} \sum_i \left(\frac{Y-R}{s_y^{1/2}} \right)^2}$.
721 Note that OMI floor noise errors (0.4% at wavelengths < 310 nm, and 0.2% at wavelengths > 310 nm) are
722 used to define RMS.



723

724 Figure 12. (a) Standard deviations of spectral fitting residuals for 14 March 2013 under clear-sky conditions
 725 and for small SZAs <math> < 40^\circ </math> (red dotted line), with the 4th order polynomial fitting of them (red solid line)
 726 called “OMPS floor noise (FN) error”. This FN error represents the minimum measurement constraint
 727 implemented in OMPS ozone fitting process. OMI floor noise error (black line) and OMPS L1B v2.0
 728 random-noise error (blue line) (orbit: 7132, cross-track: 18, along-track: 200) are also shown for
 729 comparison in the same panel. (b) OMPS FN at 302.5 nm and 340 nm as a function of SZAs (solid line),
 730 with the corresponding OMPS L1B v2.0 measurement error (dotted line).

731



732

733 **Figure 13.** Top: Comparison of RMS of fitting residuals relative to the assumed measurement errors as
 734 functions of cross-track and along-track pixels for orbit 7132 with (a) OMPS FN (first column) and (b)
 735 OMI FN (second column), respectively, with (c) their absolute differences (third column). The definition of
 736 RMS is given in Fig. 11. Middle: Comparison of average fitting residuals relative to the simulated radiances
 737 (%), which are similar to RMS, except that radiance differences are normalized to measured radiances
 738 instead of measurement errors. Bottom: Comparison of the number of the retrieval iterations.

739

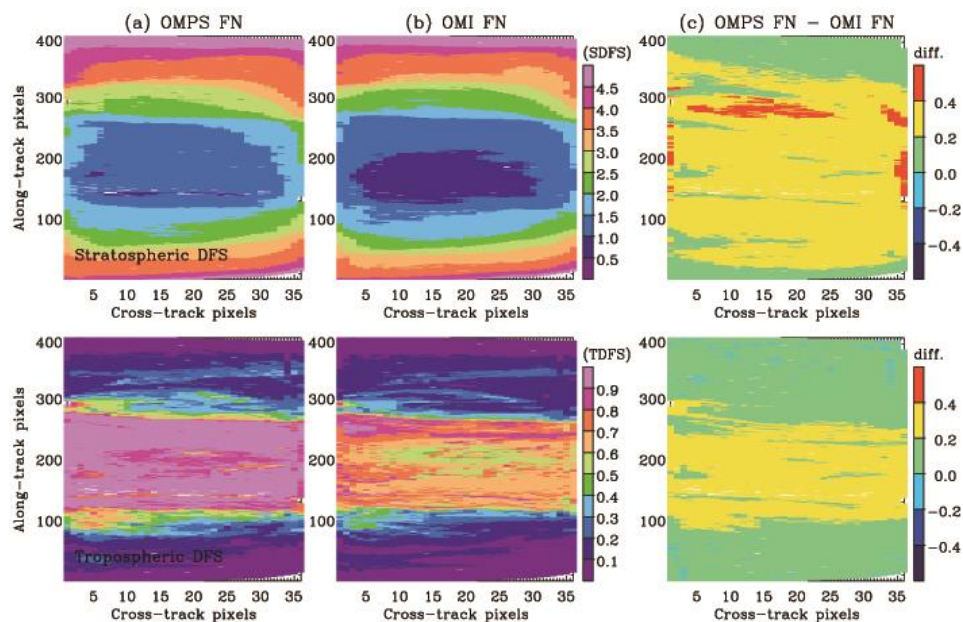
740

741



742

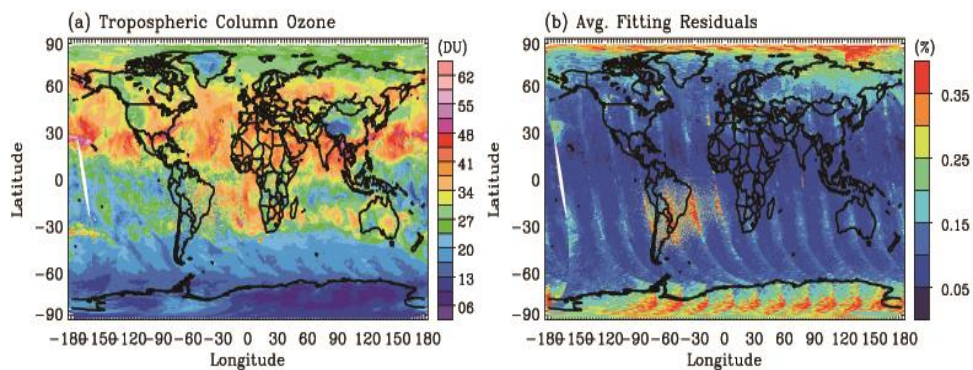
743



744

745 **Figure 14.** Same as Fig. 13, but for the integrated Degrees of Freedom for Signal (DFS) in the stratosphere
 746 (top) and troposphere (bottom), respectively.

747



748

749 **Figure 15.** (a) Same as Fig 7.b, but for improved retrievals with common mode correction and OMPS floor
 750 noise error, (b) corresponding average fitting residuals (%).